Soft Matter

PAPER

Interface-induced recirculation within a stationary microfluidic drop†

Sungyon Lee,‡[a] François Gallaire[b] and Charles N. Baroud*[a]

We study the flow within a stationary drop in a Hele-Shaw cell. The experiments are performed in a microfluidic channel, whose surface is patterned with a single hole that serves to *anchor* the drop while the outer fluid continues to flow. The recirculation pattern is found to be localized near the liquid–liquid interface for all conditions, with most of the fluid motion taking place in the curved rim of the droplet. In contrast, the drop's central region remains nearly stationary. This flow pattern corresponds to a three-dimensional recirculation on the drop surface, with the fluid moving in the direction of the outer flow on the central plane and in the opposite direction closer to the boundaries. The different velocities scale linearly with the outer fluid velocity for all geometries studied. However, the velocity on the interface is found to be lower than the driving velocity even in the case of a gas bubble, pointing to the effect of surface stresses as the underlying retardation and recirculation mechanism. This motivates the development of a Marangoni model to account for the surfactant accumulation around the downstream stagnation point. The model displays good qualitative agreement with the experimental observations for many viscosity ratios and geometries but for a well-chosen surfactant accumulation.

1 Introduction

The relative motion of a drop and the surrounding fluid leads to recirculation patterns that can serve as markers for the state of the interface[1,2] or to mix the drop's content.[3,4] They arise from the condition of non-penetration at the interface between the two fluids, which forces the streamlines to change directions when they reach the immiscible interface.[5–7] However, this simplistic picture must be modified to account for the precise device geometry[8] or physicochemical effects such as the presence of surfactants.[9]

A geometry of particular interest concerns flows in a Hele-Shaw cell, *i.e.* a channel whose depth is much smaller than its width and length. A drop in this cell is squeezed by the top and bottom boundaries but only partially fills the channel width. This classical problem has been studied in depth, both theoretically and experimentally (see ref. 10–12 for early theory and experiments). While the theoretical solutions predict that the relative velocity of an inviscid bubble should be twice the velocity of the outer fluid, this is never observed in practice. Instead, bubbles may lose their circular shapes and often travel at lower speeds than the outer fluid. Moreover, complex recirculation patterns are observed for bubbles rising in a quiescent outer fluid.[13] All of

these observations point to the effect of an uneven surfactant coverage of the interface and its redistribution due to the fluid motion.

The flows in a Hele-Shaw drop have two different origins: (i) the motion of the drop relative to the top and bottom boundaries causes the drop to "treadmill" in the depth of the cell, in order to satisfy the no-slip condition on the solid walls. (ii) The difference in velocities between the droplet and the outer fluid results in the recirculation around the drop, in order to satisfy the continuity of velocities on the interface. These flow patterns couple together to create complex motion of passive tracers which cannot be described by the depth-averaged two dimensional (2D) theory, generally used for Hele-Shaw flows. However, measurement of the fluid motion is difficult since the droplets are generally moving; hence, only qualitative descriptions exist in the literature.[13–15]

These difficulties can be addressed by the recent developments in microfluidic devices; indeed, etching a small indentation in the top boundary of a micro-Hele-Shaw cell can hold a drop or a bubble stationary against an external flow.[16,17] In addition to the technological applications of such devices to make arrays of droplet micro-reactors,[18] this approach allows us to isolate the hydrodynamic effects due to the relative flow of the outer fluid from those due to the drop motion with respect to the solid boundaries. We observe that the flow thus generated exhibits a complex three dimensional (3D) pattern on the interface, with regions of the interface traveling against the driving external flow. These recirculations are remarkably stable for different fluid combinations and geometries. We attribute them to Marangoni effects that occur due to surfactant redistribution.

[a]*LadHyX and Department of Mechanics, Ecole polytechnique, CNRS, Palaiseau, France.* E-mail: baroud@ladhyx.polytechnique.fr
[b]*LFMI, IGM, STI, EPFL, Lausanne, Suisse*
† Electronic supplementary information (ESI) available. See DOI: 10.1039/c2sm26044a
‡ Present address: Dept. of Mathematics and Applied Mathematics Laboratory, UCLA, CA, USA.

Below we begin by describing the experimental protocol in Section 2, followed by a presentation of qualitative observations, then quantitative measurements of the flow profiles in Section 3. Finally, we present a Marangoni model in Section 4 that recovers the main features of the observed profiles.

2 Experimental setup

The experiments are conducted in microfluidic channels made using soft lithography techniques. Molds of dry film photoresist are fabricated using optical lithography[20] and used to produce channels into polydimethylsiloxane (PDMS). The fabrication details are described by Fradet et al.[18] The microchannel design is shown in Fig. 1(a). It consists of a flow-focusing junction for generating droplets,[21] which leads to a wide test section. An additional inlet is used for the carrier phase and leads to the test section while bypassing the flow focusing junction. This inlet

allows us to vary the flow of the outer phase, independent of the droplet production. The microchannels are surface-treated in order to make the continuous phase completely wet; in the case of water drops in oil, the surface is treated with a dilute solution of $1H,1H,2H,2H$-perfluorodecyltrichlorosilane (Sigma-Aldrich) in FC-40 oil (3M Fluorinert).[18] In the case of air bubbles in water, the channels are used immediately after bonding with an oxygen plasma, which ensures that the surfaces are hydrophilic.

The test section is patterned with a single anchor, which corresponds to an indentation in the top surface and serves to hold the droplet stationary (see Fig. 1(b) and (c)). Upon reaching the anchor, the droplet expands into this hole, thus reducing its surface energy. It is held stationary by the gradient of surface energy as long as the drag force due to the outer fluid is small.[17] In the current experiments, we also keep the outer flow rate sufficiently low so that the droplet retains a nearly circular shape. Note also that the outer flow is not affected by the hole, which is masked by the drop that partially enters it.

Four sets of experiments are conducted in the aforementioned microchannels, with varying outer and inner fluids, as listed in Table 1. For conditions 1 through 3, a fluorinated oil (FC-40, viscosity $\mu = 4.1$ cP) is used as the carrier fluid since it does not swell the PDMS channels.[22] The FC-40 solution contains surfactants that are prepared by synthesizing a commercial lubricant oil (krytox) with a base that polarizes the hydrophilic head attached to a tail of 33 carbons.[23] The aqueous phase (experiments 1, 2, and 4) consists of distilled water with the addition of monodisperse fluorescent beads of diameter 1 μm (FluoSpheres, Invitrogen) as flow tracers, from which quantitative flow measurements are made using a commercial PIV software (DaVis, LaVision). The particles are stabilized using carboxylate groups on the surface, suitable for use in water and water-soluble solutions, and the particle solution does not contain additional surfactants. Experiment 3 also uses distilled water that contains fluorescent beads for visualization but it is mixed with glycerol to increase the aqueous phase viscosity to 5 cP.

All images are acquired through a 40× objective (Nikon, NA = 0.55, depth of field = 1.7 μm) using a fast camera (Photron Fastcam 1024PCI) at 250 or 500 frames per second. The focal plane is varied using a piezo actuator (PI instruments P-726.1CD), which could be moved in nanometer-scale steps. The experiments are performed by first locating the bottom surface of the channel, then changing the focus to observe slices within the channel; the channel depths are measured by the piezo actuator to be 30 and 50 μm. The quantitative measurements presented in Section 3.2 are based on the data for the fluid combination 1 only, while the qualitative observations apply to all experiments.
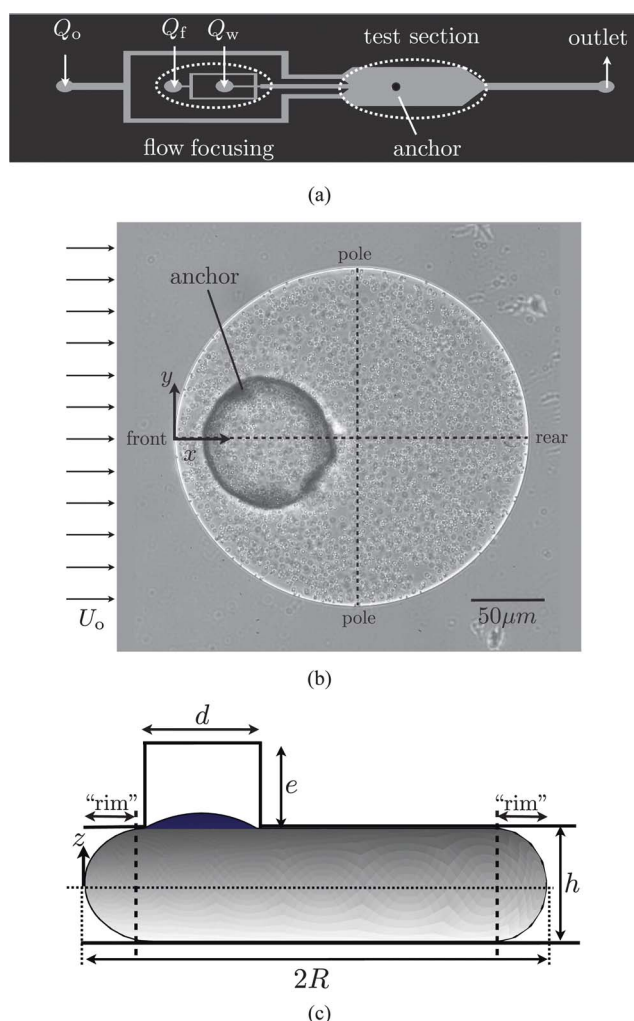

Fig. 1 (a) Schematic of a microchannel that consists of a flow focuser to generate water drops in oil and of a test section with a single anchor. The drops are produced using the inlets marked Q_f and Q_w, while the inlet marked Q_o is used to fix the carrier phase velocity in the test section (not to scale). (b) A top-down image of a pancake droplet held in place by an anchor against a mean external flow U_o. (c) Surface Evolver[19] rendering of an anchored droplet of outer radius R inside the microchannel of height h over an anchor of diameter d and of depth e.

Table 1 Fluid combinations that are tested. The quantitative measurements correspond to the conditions of row 1

	Outer phase	Inner phase
1	FC-40 + 1% surfactant A	Distilled water
2	FC-40 + 0.5% surfactant B	Distilled water + 50% glycerol ($\mu \approx 5$ cP)
3	FC-40 + 0.002 to 2% surfactant B	Distilled water
4	Distilled water	Air

3 Results

3.1 General observations

By continuity of velocity on the drop interface, the external flow triggers the fluid motion inside the stationary droplet. The resultant flow patterns are shown in Fig. 2, which displays streak-images showing the flow patterns and the associated velocity fields at two focal planes ($z = 0$ and -15 μm). Only measurements below the central plane are shown, although the symmetric recirculation pattern is also observed above the central plane. Obtaining quantitative data of the focal plane above $z = 0$ is difficult, however, as the bottom part of the drop interferes with the field of view when the droplet is viewed from below *via* the inverted microscope.

We observe that the fluid on the droplet interface moves at a speed comparable to U_o, while the fluid at the center of the drop remains nearly immobile. Indeed, the velocity decreases from its value at the edge over a distance comparable to the channel height and decays as it reaches the center of the drop. Furthermore, the fluid on the drop boundary moves in the same direction as U_o (forward) at $z = 0$ (center of the channel) but moves in the opposite direction (backward) at $z = -15$ μm. Tracking particles inside the drop reveals that the particles on the interface move from the front of the droplet to the rear at $z = 0$ and circulate back to the front on a different plane. This signifies that the anchored droplet undergoes a three-dimensional flow recirculation on the droplet boundary, despite the unidirectional flow prevailing outside in the far-field.
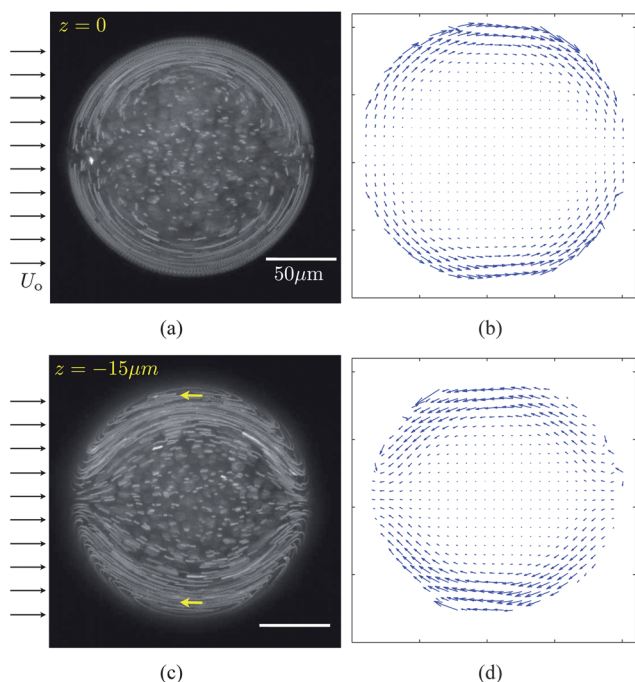

Fig. 2 Visualization of the fluorescent particles on different planes of the droplet reveals the flow patterns inside the anchored droplet. In (a) and (c), fifty successive images of time increment of 4 ms are superimposed to reveal streaklines, showing that the fast flow is confined to the drop boundary. The corresponding velocity fields are shown in (b) and (d) for mid-plane $z = 0$ and $z = -15$ μm, respectively. The velocity field in (d), in particular, shows the velocity moving in the opposite direction of the mean flow on the droplet edge.
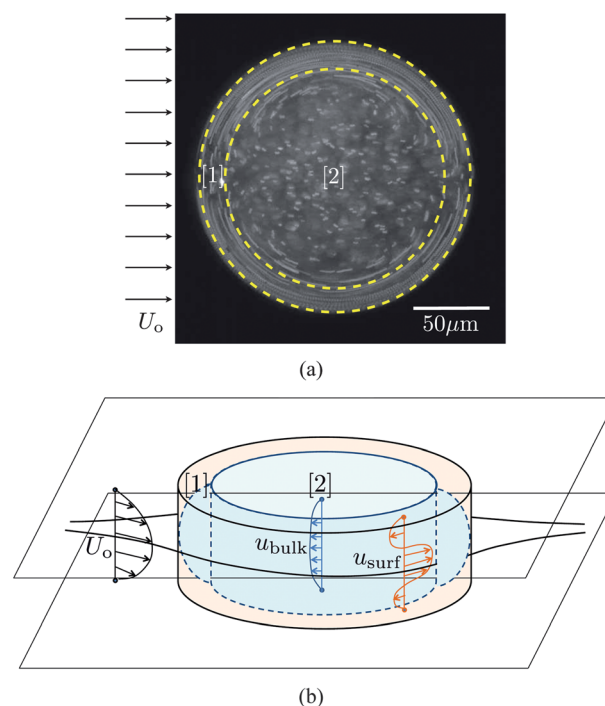

Fig. 3 (a) The fast flow region around the drop boundary is labeled as [1], while the inner region is [2]. The qualitative velocity profiles in these two separate regions are shown in (b): on the drop boundary [1], the flow moves forward at $z = 0$, and backward away from the mid-plane before vanishing on the plates; inside the inner region [2], the flow is considerably slower than in [1] and moves uniformly backward.

As sketched in Fig. 3, the flow inside the drop can be separated into two regions of interest: near the drop edge [1] and the bulk of the drop [2]. In region [1] (Fig. 3(b)), the fluid on the droplet surface at $z = 0$ moves forward. When the droplet is in contact with the channel walls at $z = \pm h/2$, the velocity must vanish to satisfy the no slip condition. Instead of decreasing monotonically, the velocity switches signs and becomes negative before reaching zero at $z = \pm h/2$. The vertical position of this velocity sign change depends on the strength of the external flow: as U_o increases, the velocity becomes negative closer to the walls, as the forward external flow affects a wider vertical distance. In region [2], the flow in the bulk of the drop moves backward for all z, before vanishing at $z = \pm h/2$.

3.2 Quantitative measurements

For the quantitative measurement of the flow inside the drop, six droplets (two drops in channels of $h = 50$ μm and four in $h = 30$ μm) are considered with U_o varying from 200 to 3000 μm s^{-1}, using the fluids listed in row 1 of Table 1. The drop radius ranges from 60 to 215 μm.

The fluid velocity on the drop boundary, u_{surf}, is measured on the droplet poles ($x = R$, $y = \pm R$), at $z = 0$ for all drops and $z = -10$ or -15 μm for $h = 30$ and 50 μm, respectively. The value of u_{surf} at the center of the channel is found to increase as $u_{surf} = 0.32 U_o$, independent of the channel height and drop radius (Fig. 4(a)). On a focal plane closer to the channel walls, the fluid on the droplet moves backward. Hence, u_{surf} measured on a plane below $z = 0$ is negative but still scales linearly with U_o with
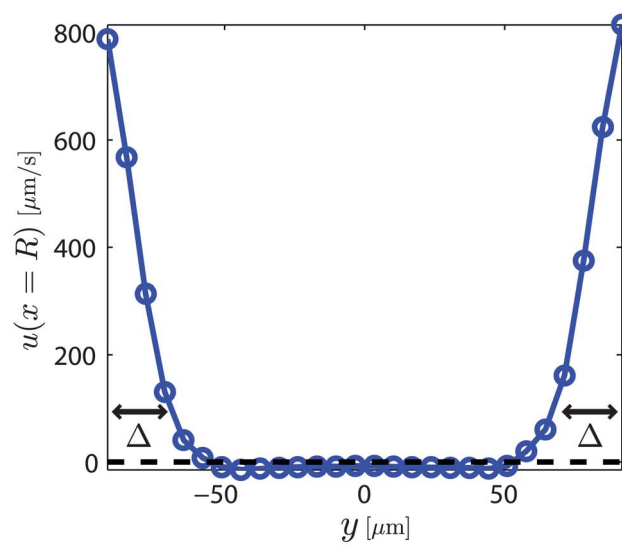
(a)
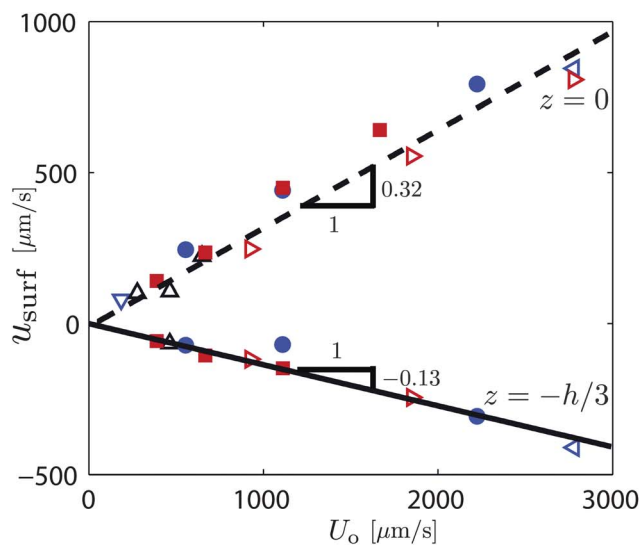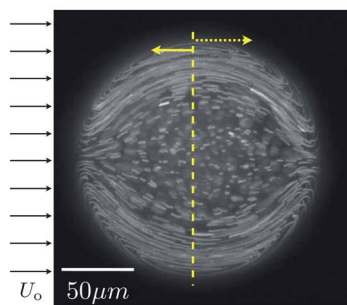
(b)   (c)

Fig. 4 (a) u_{surf} *versus* the mean external flow U_o at two different vertical planes. The surface velocity at $z = 0$ is positive and varies as $0.3U_o$. The velocity at $z \simeq h/3$ from the mid-plane is negative and scales as $0.13U_o$. (b) The schematic of the forward and backward surface velocities on the droplet. (c) The table detailing the markers used in the plot.
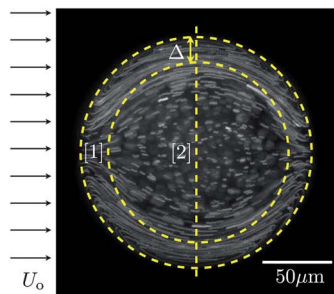

(a)

(b)   (c)

Fig. 5 (a) Horizontal velocity $u(x = R)$ measured across the width of the drop ($-R < y < R$). The distance Δ is defined as the location where $u = 0.1u_{surf}$. It corresponds to the size of the fast velocity zone [1] in (b). (c) Δ/R versus h/R. The data are well fit by a line of slope 0.53 for all flow conditions and geometries.

a slope of -0.13, shown as a solid line in Fig. 4(a). This signifies two important aspects of the recirculating flow on the drop interface. First, the magnitude of the velocity on the drop boundary varies linearly with the driving flow outside and is unaffected by the drop radius and height. Second, the fact that u_{surf} is less than U_o for a drop less viscous than the surrounding fluid suggests that a Marangoni effect may be the possible mechanism of the flow reversal on the drop interface, which will be further discussed in Section 4.

In addition to the fluid motion on the drop boundary, the flow field inside the droplet is also quantified, by first measuring the thickness of the region [1] at $z = 0$ (see Fig. 3). The decay in velocity from the edge to the center is illustrated in Fig. 5(a) by plotting the x-component of the velocity at $x = R$ across the width of the drop ($-R < y < R$), when $U_o = 2220~\mu m~s^{-1}$, the velocity on the drop surface $u(x = R, y = \pm R)$ is 800 $\mu m~s^{-1}$ and decreases to $-10~\mu m~s^{-1}$ in the bulk region.
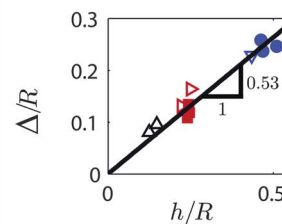
The thickness of region [1] is quantified by defining the length scale Δ as the distance over which this velocity decreases to 10% of its value on the drop surface. Δ/R is found to vary linearly with h/R with a slope of 0.53 for all drops, as shown in Fig. 5(c). Therefore, in contrast to u_{surf} that depends solely on U_o, Δ is

given by the half height of the channel independent of R and U_o. Since the distance $h/2$ corresponds to the radius of the outer "rim" of the pancake drop, as shown in Fig. 3(a), the large velocity is confined to the curved region of the drop.

In region [2] away from the drop boundary, the velocity in the drop center (u_{bulk}) is negative and smaller than both u_{surf} and U_o in magnitude. Unlike u_{surf} which undergoes a sign change in z, the velocity u_{bulk} is negative all along the channel height until it vanishes at $z = \pm h/2$. The values of u_{bulk} in Fig. 6(a) are obtained by averaging the velocities measured at $z = 0$ over the rectangular domain shown in Fig. 6(b). We observe that u_{bulk} is independent of the droplet radius and height; it varies linearly with U_o with the slope of -0.003. This further confirms that, for a stationary pancake drop, the strength of the flow on the drop boundary and inside the drop is solely determined by U_o, while the size of the fast flow region is given by the channel height.

In addition to condition 1, the same qualitative trends have been observed in other experiments listed in Table 1. In experiment 2, glycerol is added to water in order to more closely match the viscosity of the inner phase ($\mu \approx 5$ cP) to that of the outer phase (FC-40, $\mu = 4.1$ cP). The measurements show that the forward surface velocity on the poles u_{surf} scales as $0.17U_o$, while the velocity in the drop center u_{bulk} is negative and scales
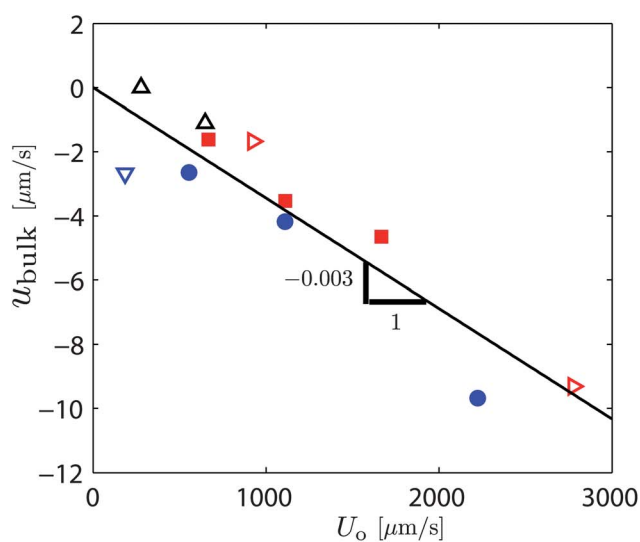
(a)
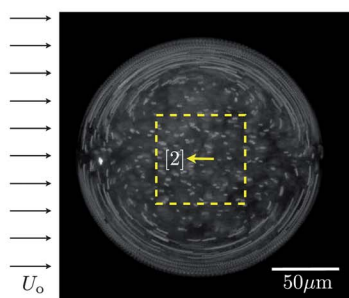
(b)

Fig. 6 (a) Bulk velocity u_{bulk} plotted against the mean flow U_o, which varies linearly with U_o, with a slope of -0.3%. (b) The value of u_{bulk} is determined by taking the mean of the velocity field inside the rectangular domain located at the center of the droplet.

as $-0.002U_o$. Compared to condition 1, in which the viscosity ratio, $\lambda = \mu_i/\mu_e = 1/4$, the increased viscous resistance further reduces the velocities, thus adding to the effects of surface flow retardation. Condition 3 corresponds to fixing λ at $1/4$ but varying the surfactant concentrations from 0.002% up to 2%. The corresponding change in surface tension, measured on a pendant drop apparatus, is from 43 mN m^{-1} to 13 mN m^{-1}, respectively. Although a complete dataset is not available, we observe that u_{surf} varies as $0.25U_o$ for the case of 2% surfactant concentration, while the bulk velocity u_{bulk} for all concentrations follows the trend of $-0.005U_o$. Thus, for both conditions 2 and 3, the pervasive surface flow retardation and the negligible center flow are evident. Equally significant is the observation of the backward flow on the interface in planes between the central plane and the walls for both experimental sets. This implies that the 3D flow reversal on the droplet interface is a robust phenomenon that occurs independent of the viscosity ratios and surfactant concentration. This is further corroborated in Section 3.3 by considering a flow around an air bubble.

3.3 Observation of an air bubble

A flow around a stationary air bubble is a simpler limit of our droplet problem, for which a well-established theoretical

prediction exists. The potential flow theory of Taylor and Saffman[10] predicts that the velocity of the outer fluid is higher near a clean air bubble than in the far-field, reaching a surface velocity of $2U_o$ on the bubble poles. Indeed, viscous stresses cannot be sustained on the interface of an inviscid bubble so any slowing down of the fluid must be due to interfacial effects. Moreover, the pressures within the bubble are in equilibrium at all times, again due to the low viscous resistance, so that any recirculation that is observed must be due to the external forcing from the outer flow. The effect of surface impurities on an air bubble is also well known. For instance, Stebe and Maldarelli[1] show that the adsorption of surfactants on the air bubble interface "rigidifies" the bubble surface, by modifying the surface rheology as well as creating Marangoni stresses.

Given these clear theoretical predictions, the experiments are repeated with an air bubble to illuminate the origin of the surface retardation as well as the 3D reversal on the droplet boundary.
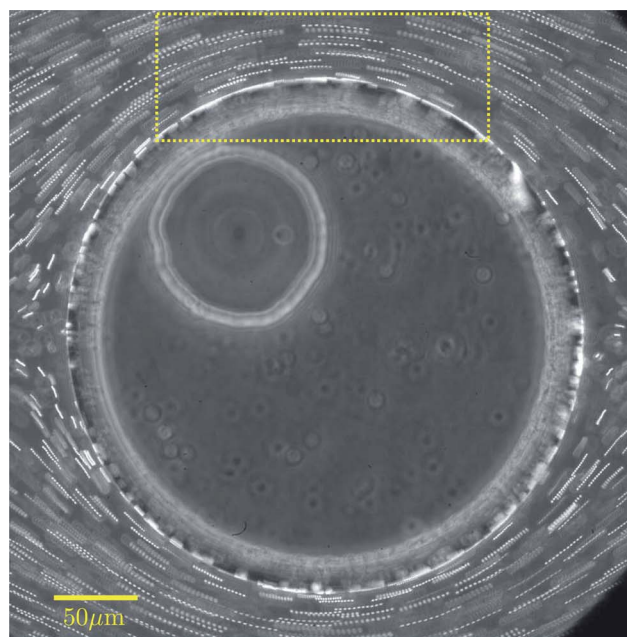
(a)
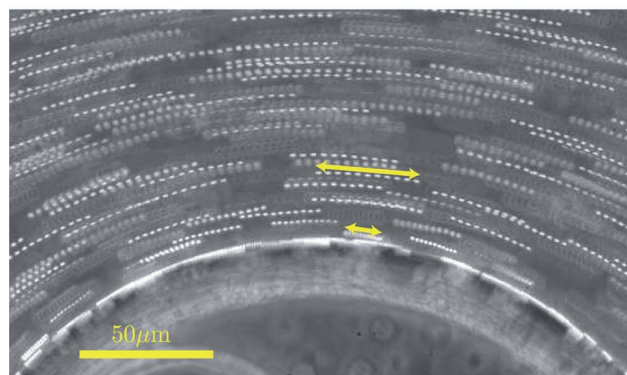
(b)

Fig. 7 (a) Superposition of 11 successive images (16 ms apart) showing particle paths around an anchored air bubble. (b) Close-up near the drop interface for the box shown in (a). Note the shorter streak lengths of the particles near the boundary compared to those away from the boundary.

To that end, we inject air into a solution of distilled water with no addition of surfactants inside the microchannel; water containing tracer particles is pushed past the air bubble continuously at an average velocity U_o (experiment 4 in Table 1). Although water is found not to wet the PDMS surface perfectly, causing the air bubble to adhere to channel walls, the bubble shape in the experiments remains smooth, with well-rounded sides, indicating that the pinning effects on the flow are minimal (see ESI movie†). The experiment is repeated for different bubble sizes and fluid velocities.

The qualitative flow pattern around the bubble is visualized by superimposing successive images of the flow (16 ms apart). Shown in Fig. 7, such superposition yields a single image that displays the paths of tracer particles, or streaklines in the steady state. Then, the length of streaklines is indicative of the local flow velocity. From the close-up view in Fig. 7(b), the streaklines appear shorter near the boundary than far away, implying a deceleration in the vicinity of the interface. At two varying flow rates, u_{surf} on the poles is measured to be 43.3% and 44.9% of U_o. This violates the theoretical prediction of flow around a clean bubble and strongly suggests the presence of surface impurities that retard the flow on the bubble interface. In addition, the flow is also observed to reverse directions on the bubble interface, as it does for anchored viscous droplets (see ESI movie,† where the focus plane slowly scans the height of the microchannel, showing the motion of solid particles near and on the bubble surface).

4 Marangoni model

In order to account for this strong retardation and the resultant flow reversal, we consider the modification of the free surface boundary condition due to the redistribution of surfactant molecules. Even when no surfactants are purposefully added to the system, as in the aforementioned bubble experiment, trace impurities are very difficult to avoid in the solutions. Thus, the outer flow past the droplet causes the surface active molecules to accumulate on the downstream stagnation point of the drop, creating a surfactant concentration gradient along the interface. This surfactant concentration gradient leads to a corresponding azimuthal surface tension gradient, as surfactants decrease the local surface tension.[9] The resultant adverse solutal Marangoni effect pulls along the surface in the opposite direction of the flow.

In the case of moving unconfined drops and bubbles, a similar retardation phenomenon has been observed in spherical bubbles, the bubble speed is reduced, while the drag changes from the Hadamard–Rybczynski value expected for an air bubble to the Stokes value expected for a solid sphere. This has also been observed in the case of pancake bubbles by Bush.[13] Following the formulation of Boos and Thess,[24] Bush uses depth-averaged Brinkman equations to account for this phenomenon, which assumes a parabolic velocity profile along the depth. This approach is also shown to work well for Marangoni driven flows with no external flow,[25] as well as in other microfluidic context.[26] However, such gap-averaged assumption is guaranteed to fail to explain the 3D flow reversal described in Section 3.

A complete theoretical treatment allowing for a reverse surface flow requires coupling the surfactant transport equation, i.e. a nonlinear advection–diffusion–adsorption–desorption equation, with the external flow. In particular, it is necessary to deduce the surface tension distribution which is consistent with both the external flow and the surfactant distribution on the droplet surface. Even in the simplest case of a surface-advection dominated regime where the adsorption–desorption dynamics is assumed instantaneous, the three-dimensional nature of the flow renders the analysis much more involved than the spherical drop case[9,27] and falls out of the scope of the present study.

In order to proceed further and qualitatively explain the 3D flow reversal, we derive a boundary layer model of the flow field, inspired by Thompson.[28] In such a model, the flow in each of the two phases is divided into an "inner" region near the boundary and an "outer" region far away. The solutions in the two regions are then matched using asymptotic methods. This model allows us to explore the three-dimensional flow patterns on the boundary while taking into account the continuity of surface stresses. In contrast to previous work, we impose a prescribed non-uniform surface tension distribution on the interface.

In order to simplify the analysis, we reduce the pancake-like geometry of the droplet to a flat circular cylinder of radius R and thickness h. Introducing the carrier fluid viscosity μ_e and far field velocity $U_o e_x$ and the droplet viscosity μ_i, the Stokes equations are made non-dimensional based on the following scales (here the "hat" ^ denotes dimensionless variables):

$$r = R\hat{r}; z = (h/2)\hat{z}; u = U_o\hat{u};$$
$$p = \frac{2U_o(\mu_e + \mu_i)R}{h^2}\hat{p}; \gamma = \frac{2U_o(\mu_e + \mu_i)R^2}{h^2}\hat{\gamma}; \quad (1)$$
$$\mu_e = (\mu_e + \mu_i)\hat{\mu}_e; \mu_i = (\mu_e + \mu_i)\hat{\mu}_i.$$

We adopt the cylindrical polar coordinate system $(\hat{r},\theta,\hat{z})$, where $\hat{r} = 0$ defines the drop's center, while $\hat{z} = 0$ corresponds to the vertical mid-plane and $\hat{z} = 1$ to the top plate. Due to the inherent symmetry of the system, only the top "quarter" of the drop (i.e., $\hat{z} > 0$ and $0 < \theta < \pi$) is considered. The velocities $\hat{u}$, $\hat{v}$ and $\hat{w}$ respectively denote the radial, azimuthal and transverse components (see Fig. 8 for the drop geometry and the notation used). We assume that the non-dimensional surface tension distribution on the drop surface takes the form

$$\hat{\gamma} = \hat{\gamma}_o - M\cos\theta, \quad (2)$$

where $\theta = 0$ corresponds to the rear of the bubble, increasing counterclockwise, and M denotes the non-dimensional magnitude of the gradient in surface tension, or equivalently the applied surface stress. Considering the rapid diffusion in the short direction $\hat{z}$, a uniform surface tension distribution along $\hat{z}$ has been assumed. Thus, eqn (2) corresponds to a linear surfactant distribution in the direction of the mean flow.

Far from the interface, the separation of scales is exploited to yield the classical Hele-Shaw equations, with the solution at the leading order in $\varepsilon = h/(2R)$:

$$\hat{U}_e = (1 - \hat{z}^2)(1 - 1/\hat{r}^2)\cos\theta, \quad (3)$$

$$\hat{V}_e = -(1 - \hat{z}^2)(1 + 1/\hat{r}^2)\sin\theta, \quad (4)$$

$$\hat{W}_e = 0, \quad (5)$$

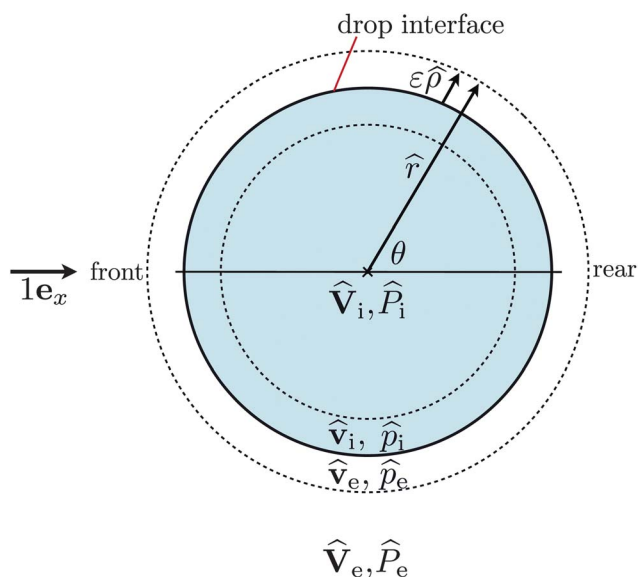$$\hat{P}_e = -2(\hat{r} + 1/\hat{r})\cos\theta. \quad (6)$$

Fig. 8 The schematic of the droplet in the polar coordinates consists of four regions: external to the drop and away from the boundary (denoted with the capital letters and a subscript "e"), an external boundary layer (lower case and subscript "e"), an internal boundary layer (lower case and subscript "i"), and internal and away from the boundary (capital letters and subscript "i"). The solid line corresponds to the drop boundary, while the areas between the solid line and the dotted lines denote the internal and external boundary layers, respectively.

The solution is chosen to satisfy the far field velocity field and the impermeability condition on the circular interface. In reality, the droplet shape is an unknown to be determined through the imposition of the normal stress jump.[17] However, as the interface does not deviate significantly from the circular shape in the present study, we will proceed with the fixed interface hypothesis, neglecting the Young–Laplace law.

The flow far from the interface inside the droplet is null at the leading order in ε:

$$\hat{U}_i = \hat{V}_i = \hat{W}_i = \hat{P}_i = 0. \tag{7}$$

This already shows that the characteristic velocities in the bulk of the droplet are at least ε times smaller than U_o.

In order to fulfill the tangential boundary conditions, let us consider a boundary layer of size ε close to the interface,

$$\hat{r} = 1 + \varepsilon\hat{\rho}, \tag{8}$$

where $\hat{\rho}$ is the rescaled radial variable in the boundary layer. The dominant balance suggests that the tangential velocity component $\hat{v}$ dominates the two other velocity components by at least an order of magnitude. In the boundary layer (inner) region of the exterior and interior fluids, the Stokes equations therefore become at the leading order

$$\frac{\partial \hat{p}_{e/i}}{\partial \hat{\rho}} = 0, \tag{9}$$

$$\frac{\partial \hat{p}_{e/i}}{\partial \hat{z}} = 0, \tag{10}$$

$$\frac{\partial^2 \hat{v}_{e/i}}{\partial \hat{\rho}^2} + \frac{\partial^2 \hat{v}_{e/i}}{\partial \hat{z}^2} = \frac{\partial \hat{p}_{e/i}}{\partial \theta}. \tag{11}$$

The asymptotic matching between the inner and outer solutions at the leading order requires

$$\lim_{\hat{\rho} \to \infty} \hat{p}_e = -4\cos\theta, \tag{12}$$

$$\lim_{\hat{\rho} \to \infty} \hat{v}_e = -2\left(1 - \hat{z}^2\right)\sin\theta, \tag{13}$$

$$\lim_{\hat{\rho} \to -\infty} \hat{p}_i = 0, \tag{14}$$

$$\lim_{\hat{\rho} \to -\infty} \hat{v}_i = 0. \tag{15}$$

Eqn (9) shows that as classically observed in boundary layers, the pressure in each boundary layer is independent of the rescaled radial variable and takes the value from the outer solutions eqn (12) and (14).

The kinematic and dynamic tangential boundary conditions on the interface are the continuity of tangential velocity and the shear stress jump, respectively,

$$\hat{v}_e = \hat{v}_i(\equiv -\hat{v}_s(\hat{z})\sin\theta), \tag{16}$$

$$\hat{\mu}_e \frac{\partial \hat{v}_e}{\partial \hat{\rho}} = \hat{\mu}_i \frac{\partial \hat{v}_i}{\partial \hat{\rho}} - (M/\varepsilon)\sin\theta. \tag{17}$$

Eqn (17) shows that the interface velocity has necessarily an azimuthal sinusoidal dependence, allowing us to define the interfacial velocity profile $\hat{v}_s(\hat{z})$ in eqn (16).

In the external fluid, the solution to eqn (11) with boundary conditions eqn (12) and (13) is

$$\hat{v}_e = \left[\sum_0^\infty b_m \exp\left(-k_m\hat{\rho}\right)\cos\left(k_m\hat{z}\right) - 2\left(1 - \hat{z}^2\right)\right]\sin\theta, \tag{18}$$

with $k_m = (m + 1/2)\pi$ and m is an integer, whereas in the internal fluid, the solution to eqn (11) with boundary conditions eqn (14) and (15) is given by

$$\hat{v}_i = \left[\sum_0^\infty a_m \exp\left(k_m\hat{\rho}\right)\cos\left(k_m\hat{z}\right)\right]\sin\theta. \tag{19}$$

Imposition of the boundary conditions yields

$$\begin{bmatrix} 1 & -1 \\ \hat{\mu}_i & \hat{\mu}_e \end{bmatrix} \begin{pmatrix} a_m \\ b_m \end{pmatrix} = \begin{pmatrix} \dfrac{-8(-1)^m}{k_m^3} \\ \dfrac{2M(-1)^m}{\varepsilon k_m^2} \end{pmatrix} \tag{20}$$

This countable family of linear equations is readily solved and the velocity profile on the surface of the drop $\hat{v}_s(\hat{z})$ is reconstructed by summation according to eqn (18) or (19) evaluated at $\hat{\rho} = 0$ and factorizing $\sin\theta$.

Typical results for a viscosity ratio of $\lambda = \mu_i/\mu_e = 1/4$ are shown in Fig. 9 for different values of the retarding soluto-capillary gradient ranging from $M/\varepsilon = 0, 2, 4, 6, 8, 10, 12$. In the absence of the Marangoni effect, the maximum surface velocity is computed to be 1.6 in comparison to the value of 2 pertaining to the $\lambda = 0$
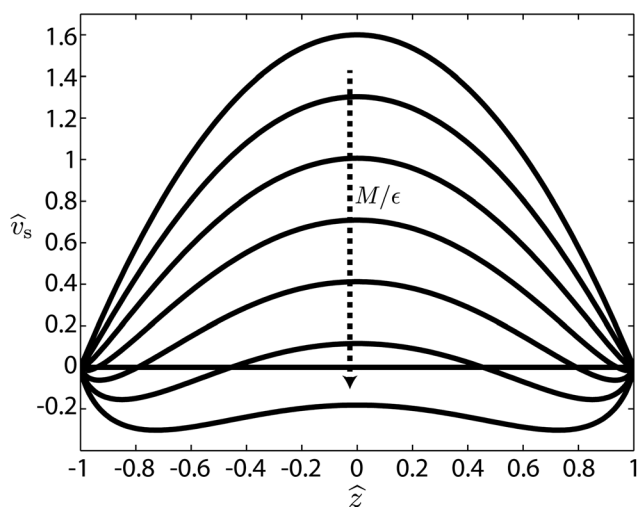
Fig. 9 Typical velocity profiles $\hat{v}_s(\hat{z})$ obtained from the boundary layer expansion in the vicinity of the droplet surface for an adverse Marangoni effect of non dimensional strength $M/\varepsilon = 0, 2, 4, 6, 8, 10, 12$; $\hat{\mu}_i = 1/5$; $\hat{\mu}_e = 4/5$.

case. For moderate Marangoni driving, the flow further decelerates until flow reversal appears for $M/\varepsilon > 4.23$ close to $\hat{z} = \pm 1$. As the Marangoni driving is further increased, the flow continues to decelerate, while the flow reversal region widens and deepens. At $M/\varepsilon = 8.7$, the maximum velocity of 0.3 and the minimum of -0.08, which recall our experimental measurements (see Fig. 4), are observed. For $M/\varepsilon > 10.75$, the entire flow reverses, and the physical assumption of negative tail-to-nose surface tension gradient is likely to break down. Similar results, with different thresholds, are observed for varying viscosity ratios including air bubbles.

It should be noted that the present boundary layer approximations are only the first step towards a rigorous asymptotic expansion which follows the line of Thompson.[28] The perspective implied by a complete asymptotic expansion will provide insight into the screening mechanism resulting in the low velocity region of the droplet center.

5   Summary and discussion

In summary, we observe a complex three-dimensional recirculation pattern within a drop that is forced by a simple unidirectional channel flow. This three dimensional motion is generic; it is observed for different drop sizes, viscosity ratios, fluid pairs, and surfactants. It always takes place in the curved rim of the droplet, near the interface, therefore leaving the fluid in the bulk of the drop nearly stationary. Although a slow central flow would be expected even from a classical two-dimensional description of the flow within the droplet,[25] the observed velocities are still an order of magnitude lower in the experiments. This can be understood by recalling that the pressure inside the drop must be constant[17] to the leading order in $h/(2r)$. The current results show that the viscous driving from the interface is further screened by the three-dimensional recirculation near the droplet edge.

Moreover, we have observed that the forward flow on the interface is slower than the driving flow even in the case of a gas

bubble. All of these observations point to the presence of surface stresses as the likely physical mechanism behind these effects. A Marangoni model, which accounts for the surfactant accumulation at the downstream end, is therefore developed. It indeed recovers the main features of the flow reversal, providing good qualitative agreement with the experimental observations for a wide range of viscosity ratios and in a limited range of soluto-capillary stresses. The generality of the recirculations in the experiments may therefore be an indication that a particular surfactant distribution arises from the interactions between advective and diffusive transport for a wide range of physical parameters.

However, our analysis cannot rule out other physical interpretations, such as effects of surface viscosity due to the presence of adsorbed contaminants. A different model of the interfacial stress that includes these dissipation mechanisms may also lead to similar flow organization but of a different physical origin. Nevertheless, our boundary-layer approach demonstrates a viable method to reconstruct the recirculation patterns on the drop interface by considering surface effects.

The experiments in this study are enabled by the new microfluidic tools that allow for quantitative flow measurements in the absence of drop migration and in the steady state. The results motivate further experiments and theoretical developments in order to better determine the underlying physical effects. From a technological point of view, they also point to limitations on mixing within the drop, which has significant implications on the application of these devices.

Acknowledgements

References

1 K. Stebe and C. Maldarelli, *J. Colloid Interface Sci.*, 1994, **163**, 177–189.
2 B. S. Hamlin and W. D. Ristenpart, *Phys. Fluids*, 2012, **24**, 012101.
3 H. Song, J. Tice and R. Ismagilov, *Angew. Chem., Int. Ed.*, 2003, **42**, 767.
4 A. Günther, M. Jhunjhunwala, M. Thalmann, M. Schmidt and K. Jensen, *Langmuir*, 2005, **21**, 1547–1555.
5 H. Hadamard, *C. R. Acad. Sci.*, 1911, **152**, 1735–1738.
6 G. Taylor, *Proc. R. Soc. London, Ser. A*, 1932, **138**, 41–48.
7 W. Rybznski, *Bull. Acad. Sci. Cracovie, A*, 1911, **1**, 40–46.
8 F. Sarrazin, T. Bonometti, L. Prat, C. Gourdon and J. Magnaudet, *Microfluid. Nanofluid.*, 2008, **5**, 131–137.
9 V. Levich, *Physicochemical Hydrodynamics*, Prentice Hall, Englewood Clifs, NJ, 1962.
10 G. I. Taylor and P. G. Saffman, *Q. J. Mech. Appl. Math.*, 1959, **12**, 265–279.
11 T. Maxworthy, *J. Fluid Mech.*, 1986, **173**, 95–114.
12 A. R. Kopf-Sill and G. Homsy, *Phys. Fluids*, 1988, **31**, 18–26.
13 J. Bush, *J. Fluid Mech.*, 1997, **352**, 283–303.
14 D. Burgess and M. R. Foster, *Phys. Fluids A*, 1990, **2**, 1105–1117.
15 S. R. K. Maruvada and C.-W. Park, *Phys. Fluids*, 1996, **8**, 3229–3233.
16 P. Abbyad, R. Dangla, A. Alexandrou and C. Baroud, *Lab Chip*, 2011, **11**, 813–821.
17 R. Dangla, S. Lee and C. N. Baroud, *Phys. Rev. Lett.*, 2011, **107**, 124501.

18 E. Fradet, C. McDougall, P. Abbyad, R. Dangla, D. McGloin and C. N. Baroud, *Lab Chip*, 2011, **11**, 4228–4234.

19 K. Brakke, *Surface Evolver Manual*, 2008, http://www.susqu.edu/facstaff/b/brakke/evolver/evolver.html.

20 K. Stephan, P. Pittet, L. Renaud, P. Kleimann, P. Morin, N. Ouaini and R. Ferrigno, *J. Micromech. Microeng.*, 2007, **17**, N69–N74.

21 S. Anna, N. Bontoux and H. Stone, *Appl. Phys. Lett.*, 2003, **82**, 364–366.

22 R. Dangla, F. Gallaire and C. N. Baroud, *Lab Chip*, 2010, **10**, 2032–2045.

23 J. Clausell-Tormos, D. Lieber, J. Baret, A. El-Harrak, O. Miller, L. Frenz, J. Blouwolff, K. Humphry, S. Köster and H. Duan, *et al.*, *Chem. Biol.*, 2008, **15**, 427–437.

24 W. Boos and A. Thess, *J. Fluid Mech.*, 1997, **352**, 305–320.

25 F. Gallaire, P. Meliga, P. Laure and C. N. Baroud, *Phys. Fluids*, 2012, submitted.

26 C. N. Baroud, J.-P. Delville, F. Gallaire and R. Wunenburger, *Phys. Rev. E: Stat., Nonlinear, Soft Matter Phys.*, 2007, **75**, 046302.

27 R. S. Subramanian and R. Balasubramaniam, *The Motion of Bubbles and Drops in Reduced Gravity*, Cambridge University Press, 2001.

28 B. W. Thompson, *J. Fluid Mech.*, 1968, **31**, 379–395.